

# Hydrogen fuel cells for aviation?

A potential analysis comparing different thrust categories

**Marc Schmelcher, Jannik Häßy**

**Marc.Schmelcher@dlr.de**

German Aerospace Center (DLR)  
Institute of Propulsion Technology  
Cologne  
Germany

## ABSTRACT

The emission of greenhouse gases is causing a rising global average temperature and extreme climate events. The European Commission has set ambitious goals until 2050 to reduce CO<sub>2</sub> and NO<sub>x</sub> emissions in aviation. But to reach these goals revolutionary developments are necessary since the optimization potential of conventional technologies is limited. Propulsion systems powered by proton exchange membrane fuel cells (PEMFC) emit only water vapor and would reduce the climate impact of aviation. Therefore, the feasibility of hydrogen powered PEMFC propulsion systems for the application in different aircraft categories is analyzed.

A basic fuel cell model is integrated in the virtual engine framework GTlab. The influence of major design parameters on the behavior of the system is analyzed. Fuel cell-based propulsion systems are designed for four aircraft applications that differ in flight operating conditions, payload and range. The designed hydrogen fuel-cell-powered propulsion systems are compared to the corresponding conventional kerosene-fueled engines. The implications on system efficiency, size and mass including the hydrogen storage are discussed.

High operating temperatures (e.g. 180°C) are crucial to keep the cooling system at a reasonable size. For a current technology level, a typical regional aircraft application with a mission range of 1320 km shows the lowest weight increase (18% of TOW<sub>ref</sub>). Assuming a technology level for entry into service in 2040, the mass increases by only 7.4%. For a short- to mid-range scenario with future assumptions the mass increases by 55% of TOW<sub>ref</sub>. These results are achieved neglecting the impacts on the aircraft design. Anyhow, a fuel cell powered propulsion system is not convenient for aircraft with high thrust requirements. Combined with the results of two additional scenarios (general aviation, commuter aircraft), this work is the basis for future research in fuel cell-based propulsion systems in civil aviation.

**Keywords:** proton exchange membrane fuel cell; powertrain; potential analysis; electric propulsion; hydrogen; shortrange; midrange; commuter; general aviation

## NOMENCLATURE

DLR	German Aerospace Center
EIS	Entry into service
EOF	End of field
GTlab	Gas Turbine Laboratory
HT	High temperature
LT	Low temperature
MTO	Maximum take-off
(M)TOW	(Maximum) take-off weight
PAX	Passengers
PE	Power electronics
PEMFC/PEM	Proton exchange membrane fuel cell
RCD	Relative current density
SOFC	Solid oxide fuel cell
act	activation
conc	concentration
evap	evaporation
ins	insulation
ohm	ohmic
paras	parasitic
rev	reversible
temp-rise	temperature rise
tot	total

## Symbols

A	Surface
ASR <sub>ohm</sub>	Area specific resistance
C	Cathode
F	Faraday constant
F <sub>N</sub>	Net thrust
H <sub>2</sub>	Hydrogen
LHV	Lower heating values
Ma	Mach number
NTU	Number of transfer units
P <sub>max</sub>	Maximum power density
P	Temperature effectiveness
P / PW	Power
$\dot{Q}$	Heat flow
R	Molar gas constant
R	Heat capacity ratio
T	Temperature
U	Voltage
c	Empirical constant for concentration losses
c <sub>0</sub>	Air speed
$\Delta h$	Specific enthalpy difference
i	Inner
j	Current density (A/cm <sup>2</sup> )
j <sub>0</sub>	Exchange current density
j <sub>l</sub>	Limiting current density
j <sub>max</sub>	Current density for maximum power density
m	Mass
$\dot{m}$	Mass flow
p	Propulsion
p	Pressure
r <sub>boiloff</sub>	Boiloff-rate
z	Number of transferred electrons
$\alpha$	Charge transfer coefficient

$\delta$	Thickness
$\eta$	Efficiency
$\lambda$	Stoichiometry
$\lambda$	Thermal conductivity
$\varphi$	Length to diameter ratio of hydrogen tank

## 1.0 INTRODUCTION

The latest natural disasters, like the flood in Germany in summer 2021, show that the impact of climate change on our daily live increases [1]. To stop climate change we have to decrease the emission of greenhouse gases significantly. Aviation produces 3% of the worldwide CO<sub>2</sub> emissions and there is a trend of increasing travel activities worldwide, except during the ongoing Covid crisis [2,3]. To reduce the climate impact of aviation, the European commission has set ambitious goals in the “Flightpath 2050”-Report in 2011. CO<sub>2</sub> emissions have to be reduced by 75% and NO<sub>x</sub> emissions by 90% compared to aircraft from year 2000 [4].

Since purely evolutionary developments in civil aircraft engines might not reach the goals in time, revolutionary concepts are strongly investigated. Battery-electric, hydrogen powered and hybrid systems have become very popular in research during the last 15 years [5–9]. Most of research and development regarding fuel cells aims at small scale drones and aircraft (PAX < 5) like the HY4 aircraft [10] and HES Element One [11], or auxiliary power units [9,12]. But, to the knowledge of the author, there are no publications that compare the potential of hydrogen fuel cell driven propulsion systems in aviation, considering different aircraft categories.

Therefore, this paper analyzes the potential of fuel cells in aviation for different aircraft categories and outlines the main challenges regarding the design and integration. The storage of hydrogen as energy carrier is investigated in research regarding direct combustion of hydrogen as well [13,14]. In this paper, the focus is the power and propulsion system and not the hydrogen storage.

Current fuel cell technologies, cooling concepts and hydrogen storages are briefly introduced. The developed models for constituting elements of the fuel cell-based propulsion system are presented. All single component models are combined with existing conventional component models to form a proton exchange membrane fuel cell (PEMFC) powered propulsion system. This system model is used for different studies to identify important design parameters in the aviation context. Conducted mission analysis for different aircraft categories are presented and discussed. Main advantages but also disadvantages of a PEMFC engine related to aircraft size and mission are determined. Additionally, key aspects for future component developments are outlined.

## 2.0 STATE OF THE ART

PEMFCs are the dominating fuel cells in the transportation sector due to their good start-up behavior and quick response on alternating loads. Compared to other fuel cell types, they reach a high efficiency combined with a high power density. Solid oxide fuel cells (SOFC) have higher efficiencies and power densities but are barely tested in transportation because of slow start-up and the use of brittle ceramics [15]. Low temperature PEMFCs (LTPEMFC) are commercial standard today but high temperature PEMFC (HTPEMFC) are under research as well. The higher operating temperature of HTPEMFC of 120-180°C facilitates cooling of the system and reduces water management problems compared to LTPEMFC (50-80°C) [16].

Cooling of the system is challenging since fuel cells generate a lot of waste heat but just a small fraction is removed by the exhaust stream. Therefore, the fuel cell system has to be additionally cooled by a coolant. For applications with power above 5kW the use of air cooling with low specific heat capacity is insufficient and liquid cooling has to be considered [17,18]. In this case the liquid coolant has to transmit the heat to the environment in a heat exchanger (cooler) which results in an extra weight and volume

penalty. Large temperature differences between coolant and ambient improve the cooler performance and decrease its dimensions. This is one of the main drivers for research in the HTPEMFC technology.

On the one hand, hydrogen ( $H_2$ ) as energy carrier has a high gravimetric energy density of 33.3 kWh/kg compared to 12 kWh/kg for kerosene. On the other hand, at standard conditions the density of  $H_2$  (approx.  $0.089 \text{ kg/m}^3$ ) is more than 8000 times smaller than the density of kerosene (approx.  $800 \text{ kg/m}^3$ ). Physical storage techniques increasing the density, where hydrogen is stored at high pressure (gaseous high-pressure storage) or cryogenic in liquid form below  $-252.76^\circ\text{C}$ , are most explored and used today in transportation. For pressurized tanks, a pressure of 350 bar or 700 bar is state of the art [19]. The gravimetric efficiency of a tank system is defined by equation 1 and represents the penalty of tank system mass on the total hydrogen storage mass.

$$\eta_{grav.} = \frac{m_{H_2}}{m_{H_2} + m_{tank\ system}} \quad (1)$$

For high-pressure tanks the currently achieved gravimetric efficiency varies between 3–10%, depending on the pressure level and materials [19–22]. Using cryogenic storage a large variance is found in literature with a range from 6 % according to HÖHLEIN [23] to 75% according to VERSTRAETE [24] or GOMEZ and SMITH [14]. This large range is due to the strong dependency on tank capacity and will be further explained in chapter 3.3. Other storage options like metal hydride storage technique or storage in carbon nanotubes are not further discussed, since they are not tested for large-scale applications [21].

### 3.0 METHODS

The model of the fuel cell driven propulsion system is developed using GTlab, DLRs virtual propulsion framework [25]. New component models, like the fuel cell stack and cooler, are added to the GTlab environment. The underlying model assumptions and formulas are presented in this section. The other required components to model the overall propulsion system, like the intake, nozzle or electric motor, are already implemented and therefore not further discussed in this paper. However, the full propulsion system model is presented in subsection 3.4. This model is used to perform parametric studies investigating different design parameter in section 4.1.

In addition to the propulsion system model, a hydrogen tank model is implemented. It estimates mass and dimensions of the tank for a required capacity (section 3.3). This model is used during the mission analysis of different aircraft types.

#### 3.1 Fuel cell model

PEMFCs produce electric power according to the overall reaction of hydrogen with oxygen to water. This reaction is split into two partial reactions which are spatially separated by a proton exchange membrane. Electrons cannot pass this membrane and therefore an electric current is established by the electron transport through a bypassed electric circuit. Fuel cells produce not only electrical power but also heat in the same order of magnitude. This heat has to be actively removed to maintain the operating temperature and prevent overheating. In contrast to combustion engines, the heat is not emitted through the exhaust stream.

A basic 0D-model is used to evaluate the fuel cell behavior in an aircraft propulsion system. This model is based on the books by O'HAYRE et al. [20] and DICKS et al. [26]. It provides information on required fuel and air mass flow to fulfill a given power demand. The produced heat, the actual cell voltage and the cell current density (current per cell surface area) are modelled as well. In addition, the cell efficiency can be calculated and a sizing routine for design calculations is included, assuming a maximum power density of a cell and scaling of single cells to full stacks.

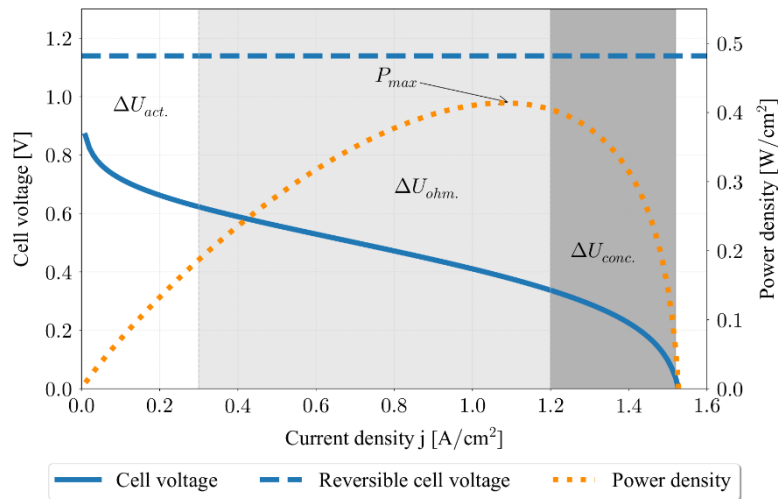


Figure 1 Representative characteristic polarization and power density curve of a PEM fuel cell

The relation between voltage, current density and power density is shown for a representative cell in Figure 1. Without losses, a fuel cell provides a constant reversible cell voltage based on the Gibbs free energy released by the reaction for all current densities. This voltage is close to 1.18 V for hydrogen PEMFCs at approx. 80°C. The reversible voltage is marked as a blue dashed line in Figure 1. The real cell voltage (blue line) is significantly smaller for all current densities. This voltage curve is often called characteristic polarization curve of a fuel cell. At low current densities up to 0.3 A/cm<sup>2</sup>, the losses are dominated by the activation energy of the reaction. For a large part of the characteristic curve (0.3-1.2 A/cm<sup>2</sup>) the voltage decreases nearly linear with current density according to dominating ohmic losses. At high current densities the voltage drops to zero due to dominating concentration losses, induced by insufficient concentrations of reactants at the electrodes. This characteristic polarization curve is dependent on fuel cell type (HT/LT), fuel cell materials, flow channels, fluid temperatures (T), pressures (p) and mass flow stoichiometry (λ). While it is outside the scope of this work to analyze different fuel cell materials and flow geometries, the effect of the variation of fluid properties (T, p, λ) and the PEMFC-type (HT/LT) is assessed using a simplified model. Therefore, a parametric model defined by equation 2 is used to calculate the characteristic polarization curve, where the above-mentioned properties influence the parameters in the equation.

$$\begin{aligned}
 U(j) &= U_{rev} - \Delta U_{act.} - \Delta U_{ohm.} - \Delta U_{conc.} \quad (2) \\
 &= U_{rev} - \frac{RT_{PEM}}{\alpha z F} \ln\left(\frac{j}{j_0}\right) - j * (ASR_{ohm}) - c \ln\left(\frac{j_l}{j_l - j}\right)
 \end{aligned}$$

The parameters  $\alpha$ ,  $j_0$ ,  $ASR_{ohm}$ ,  $c$  and  $j_l$  are calibrated using experimental data of LTPMEMFCs and HTPMEMFCs presented by LÖHN [27]. The experiments have been conducted before 2010 and do not represent the latest technology. The data used for calibration include various characteristic lines for different temperatures, pressures, and stoichiometries and to the knowledge of the authors there is no other more recent set of comparable data available in the public domain. To take into consideration improvements for future fuel cell stacks, a scaling factor can be applied on the fuel cell voltage to assume a higher voltage and thus a higher efficiency. The calibrated parameters of equation 2 can be found in the appendix.

When the location of the operating point on the characteristic curve is known, mass flows of hydrogen and air, electric power and heat output can be calculated by cell voltage and current density. Therefore, the reaction equation of hydrogen and air to water is used together with some basic thermo-electrical equations. Please refer to O'HAYRE et al. [20] and DICKS et al. [26] for further information.

During off-design calculations the operating point on the polarization curve is a result of the stack sizing during design and the actual operating conditions. To size the fuel cell, the relative current density (RCD) has to be selected as a fuel cell design parameter (see equation 3).

$$RCD = \frac{j}{j_{max}} \quad (3)$$

where  $j_{max}$  is defined as the current density with the highest power density defined by equation 4:

$$P_{max} = U(j_{max}) * j_{max} \quad (4)$$

In Figure 1 the according power density curve (orange dashed line) shows the point of  $P_{max}$ , where to  $j_{max}$  corresponds. During the design of a fuel cell driven propulsion system, the value of RCD will be within the range of 0 to 1. Values towards 0 lead to high efficiencies due to high cell voltage, but the designed stack will have a low power density. In contrary, pushing the value to 1 will increase power density but lower the efficiency. Values above 1 are possible but not reasonable, since power density and efficiency decrease rapidly in this region.

For the purpose of this paper, a simple approach is used to estimate mass and volume of the fuel cell stack including its balance of plant components. Therefore, literature values for specific volumetric and gravimetric power density of a fuel cell stack are taken. They are multiplied with the maximal possible power ( $RCD = 1$ ) of the designed fuel cell stack. This will not consider scaling effects on specific volumetric and gravimetric power density, but according to [20] the effect is small anyway. All assumptions of this model are given in the appendix.

### 3.2 Cooling system model

Fuel cells produce a significant amount of heat that has to be transferred to the ambient to maintain the operating temperature. Furthermore, the cathode and anode inlet streams have to be preconditioned to provide the fluids at reasonable temperature, close to the operating temperature of the fuel cell stack. Therefore, a liquid cooling circuit that connects the fuel cell stack with an ambient heat exchanger is considered for the model.

Starting at the fuel cell stack, the coolant is heated by the excess heat of the fuel cells and is used to precondition the air stream at the inlet of the cathode. The cathode air has to be heated or cooled depending on the operating temperature of the stack and ambient conditions. Then, the coolant is used to precondition the anode hydrogen inlet stream. In case of cryogenic storage, the hydrogen flow can be used as a heat sink to cool down the coolant while the hydrogen is heated to operating conditions. To close the circuit the coolant is cooled down by ambient air and an electrically driven pump is used to compensate pressure losses in all components.

The preconditioning of the fuel cell inlet streams and the heat transfer from the stack to the coolant are considered using energy balances around the stack. Necessary heat exchangers for preconditioning and heat transfer from the fuel cell stack to the coolant are not modeled, since a detailed modelling of these processes would be beyond the scope of this paper. In contrast, the ambient heat exchanger is modelled with a low order model since its dimensions are assumed to be significant larger and its performance depends strongly on the flight and atmospheric conditions.

The model of the ambient heat exchanger is based on the P-NTU method, which is a common pre-design method for heat exchangers in industry [28–30]. The basic assumptions are just briefly discussed.

The P-NTU method is based on three nondimensional parameters to describe the transferred heat per surface area depending on the flow geometry. The temperature effectiveness  $P$  (eq. 5), the number of transfer units  $NTU$  (eq. 6) and the heat capacity ratio  $R$  (eq. 7). They are consistently defined for both fluid sides labeled by the indices (1 and 2).

$$P_1 = \frac{T_{1,out} - T_{1,in}}{T_{2,in} - T_{1,in}} \quad P_2 = \frac{T_{2,in} - T_{2,out}}{T_{2,in} - T_{1,in}} \quad (5)$$

$$NTU_1 = \frac{UA}{\dot{m}_1 c_{p,1}} \quad NTU_2 = \frac{UA}{\dot{m}_2 c_{p,2}} \quad (6)$$

$$R_1 = \frac{\dot{m}_1 c_{p,1}}{\dot{m}_2 c_{p,2}} \quad R_2 = \frac{1}{R_1} \quad (7)$$

To calculate the parameters  $P$ ,  $NTU$  and  $R$ , a constant overall heat transfer coefficient  $U$  and constant specific heat capacity for both fluids  $c_{p,i}$  are assumed. Furthermore, the same heat transfer surface area  $A$  is considered for both sides. The temperatures at inlet and outlet of both fluid sides of the heat exchanger ( $T_{i,in/out}$ ) and the mass flow of both fluid sides ( $\dot{m}_i$ ) are part of the model as well. The three nondimensional parameters are related to each other by a correlation that depends on the flow arrangement. A single pass crossflow heat exchanger with both fluids mixed is assumed, which is a conservative assumption for the heat transfer efficiency. The corresponding numerically derived correlation is:

$$P_i = \left( \frac{1}{1 - \exp(-NTU_i)} + \frac{R_i}{1 - \exp(-R_i NTU_i)} - \frac{1}{NTU_i} \right)^{-1} \quad (8)$$

Equations 5 to 8 are used for design and off-design calculations of the heat exchanger. During design calculations, a target value for the temperature effectiveness  $P_{target}$  on the air side is set and the heat transfer surface area  $A$  is iteratively adjusted. This heat exchanger area  $A_{design}$  is constant for the off-design calculations and then the temperature effectiveness is a result variable.  $A_{design}$  is also used to estimate volume and mass of the heat exchanger by assuming a surface to volume ratio, a wall thickness and material density (see Appendix).

### 3.3 Hydrogen tank model

It is important to take the hydrogen tank into consideration during the mission analysis to recognize the effect of different system efficiencies on overall system weight and volume including the hydrogen tank. As described in chapter 2.0 hydrogen has a significantly lower volumetric energy density than kerosene and therefore cryogenic or compressed tanks are needed to increase its density. These tanks are significantly larger and heavier compared to integral wing tanks for kerosene of conventional aircraft.

To keep complexity limited, all tanks are designed as cylindrical tanks with spherically shaped domes. The only design variable for the geometry is the ratio of cylinder length to diameter called  $\phi$ . Using the density of hydrogen at the design state (cryogenic liquid or compressed gas), the inner volume of the tank can be calculated with the required hydrogen mass.

Barlow's formula is used to estimate the thickness of the cylindrical and spherical shaped structures of the tank according to [21]. For this paper, a safety factor of 2 is assumed and various materials with different properties are analyzed. The inner pressure is set to the pressure of the stored hydrogen and the outer pressure is set to zero Pascal to get conservative results even at high flight altitudes.

In case of compressed hydrogen storage, the model is calculated with inner pressures of 350 bar or 700 bar. In case of cryogenic hydrogen storage, the model is calculated with an inner pressure of 1.5 bar. This low pressure leads to significantly lower structural thickness when using cryogenic storage. But, an additional insulation thickness has to be considered in this case.

It is not possible to fully insulate a cryogenic tank and there is always a heat flow ( $\dot{Q}_{tank}$ ) from the outer side to the cryogenic inner side. This leads to an evaporation of the liquid hydrogen and increasing pressure. To prevent structural damage, a venting valve is required to ensure constant pressure. The ventilation mass flow ( $\dot{m}_{boiloff}$ ) is called boiloff and has to be limited to minimize fuel loss. In this study, a maximum boiloff-rate ( $r_{boiloff}$ ) of 0.1% per hour is allowed. The allowed incoming heat flow can be calculated by equations 9 and 10. Therefore, the evaporation enthalpy  $\Delta h_{evap,H_2} = 445.6$  kJ/kg of

liquid hydrogen at 1.5 bar is used and an enthalpy difference due to temperature rise of  $\Delta h_{temp-rise,H2} = 490 \text{ kJ/kg}$  is assumed.

$$\dot{m}_{boiloff} = m_{H2} * r_{boiloff} \quad (9)$$

$$\dot{Q}_{tank} = \dot{m}_{boiloff} * (\Delta h_{evap,H2} + \Delta h_{temp-rise,H2}) \quad (10)$$

The insulation thickness ( $\delta_{ins}$ ) is estimated by Fourier's law in form of equation 11. The mean temperature outside the tank is assumed to be  $T_{m,out} = 250 \text{ K}$  and the mean temperature inside the tank is assumed to be  $T_{m,in} = 61 \text{ K}$ . The thermal conductivity ( $\lambda_{ins}$ ) depends on the chosen insulation type and the surface area  $A_{ins}$  is taken from the structural calculations.

$$\delta_{ins} = \frac{A_{ins} * \lambda_{ins}}{\dot{Q}_{tank}} * (T_{m,out} - T_{m,in}) \quad (11)$$

With the insulation thickness, its volume and mass can be calculated using the density of the insulation material. Finally, the structural and insulation sizing are combined to get the overall tank size.

### 3.4 Propulsion system model

The models for the fuel cell and cooling system described in chapters 3.1 and 3.2 are integrated into GTlab. The resulting overall propulsion system model used in this study is presented in Figure 2. It consists of three parallel air paths which interact via the cooling circuit and the electrical circuit. The first air path (top of Figure 2) is used to model the ambient air heat exchanger which is needed as a heat sink for the cooling circuit. To overcome pressure losses in the heat exchanger, a compressor is used upstream of the heat exchanger. The compressor and the coolant pump are powered by electric motors that are supplied directly from the fuel cell stack. The heated air flows through a nozzle downstream of the heat exchanger and depending on the flight conditions, it produces some extra thrust.

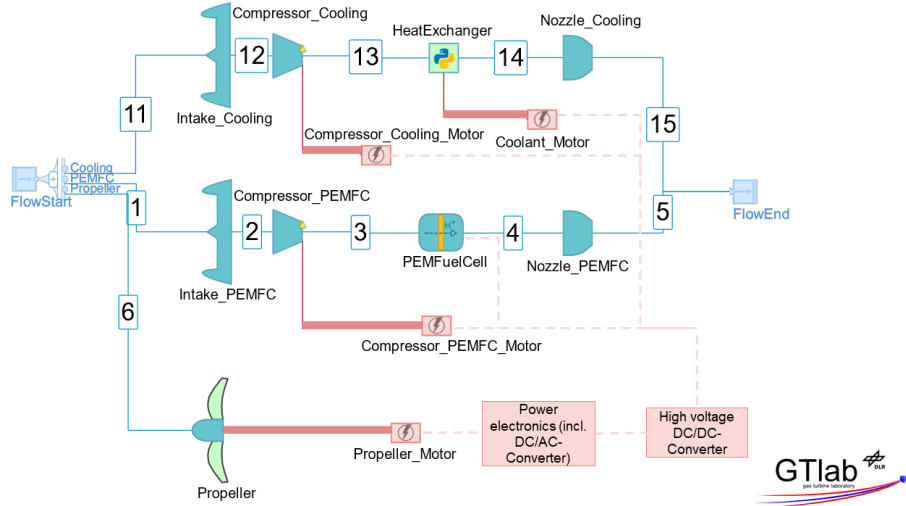


Figure 2 Model of the hydrogen fuel cell driven propulsion system in GTlab

The second air path (mid of Figure 2) is the cathode air. As described in section 3.1, the efficiency of the fuel cell depends on the operating pressure. Therefore, a compressor is required to compress the cathode air before it enters the fuel cell stack, especially at high flight altitudes. This compressor is again powered by an electrical motor supplied by the PEMFC. After leaving the fuel cell, the humidified and slightly heated air flows through a nozzle.

The compressors of both paths are calculated with a constant polytropic efficiency in every operating point. A map-based approach for the performance calculation did not converge as it is discussed in section 4.1.6.



The third air path (bottom of Figure 2) represents the path through the propulsor, in this case a propeller, which is driven by an electric motor. Power electronics are considered to generate alternate current at constant voltage for the propulsion motor. This path produces most of the thrust but the other paths also contribute with small thrust fractions.

The electric components are all modelled using a constant efficiency (see Appendix). Since this model deviates from a traditional gas turbine engine, some helpful definitions are introduced here, that will be used in the Results & Discussion chapter 4.0. The electric power provided by the PEMFC is called  $P_{PEMFC}$ . The parasitic losses  $P_{paras}$  are the sum of the power consumed by the two compressor motors and the coolant motor. These parasitic losses reduce the power from the PEMFC to the net power  $P_{net}$ . The power losses in the power electronic elements (PE) and the propulsion motor reduce the net power to the power at the propulsion shaft  $P_{shaft}$ . Finally, this shaft power is converted into thrust by a propeller or an electric fan. An internal, propulsion and total efficiency of the propulsion system are defined in equations 12-15.

$$\eta_i = \frac{P_{shaft}}{P_{PEMFC}} = \frac{P_{shaft}}{P_{PE}} * \frac{P_{PE}}{P_{net}} * \frac{P_{net}}{P_{PEMFC}} = \eta_{motor} * \eta_{PE} * \eta_{paras} \quad (12)$$

$$\eta_{paras} = \frac{P_{PEMFC} - \frac{P_{paras}}{\eta_{motor}}}{P_{PEMFC}} \quad (13)$$

$$\eta_p = \frac{F_N * c_o}{P_{shaft}} \quad (14)$$

$$\eta_{tot} = \frac{F_N * c_o}{\dot{m}_{H_2} * LHV_{H_2}} = \eta_p * \eta_i * \eta_{PEMFC} \quad (15)$$

### 3.5 Mission analysis

In this section, the most important assumptions and constraints of the mission analysis are introduced. Thrust requirements and flight conditions for the powertrain sizing of the different aircraft types are given as input to the propulsion model. The take-off condition is used as design point since it is the most critical point for a fuel cell propulsion system. High power demand and low ambient temperature difference push the fuel cell stacks and the thermal management system to its limits. Nevertheless, the RCD design value of the fuel cell and the  $P_{target}$  design value of the heat exchanger are adjusted to ensure a safe operation in all flight phases (Take-Off, End of Field, Top of Climb, Cruise). Moreover, the variation of system weight and volume or overall fuel consumption depending on RCD and  $P_{target}$  are evaluated during the analysis.

For each designed propulsion system, the overall fuel consumption is calculated by Breguet's range equation using the specific fuel consumption in the different flight phases. The block fuel is used to estimate size and mass of the hydrogen tank system. Therefore, the maximum range of the reference aircraft is used to size the tank and the mission range is used to calculate the fuel weight. The main assumption during the sizing of the tank is to use a constant fuselage diameter of the reference aircraft and to adjust the tank length according to its capacity. Additionally, a buffer battery for dynamic operations is sized with a capacity to power the system for two minutes at take-off.

In combination with mass and volume estimations for all other components of the propulsion system described in section 3.4, a direct comparison to the reference system is made. A further iterative consideration of adapted aircraft designs due to the new propulsion system is out of the scope of this work. Therefore, the result of this analysis is by no means a consistent aircraft design. The used thrust requirements are not consistent with the resulting aircraft mass and aerodynamics. Furthermore, a weight & balance analysis of an aircraft with hydrogen tanks and a fuel cell propulsion system is missing. But the potentials can be identified with this simple approach and are investigated as described in the next section.

## 4.0 RESULTS & DISCUSSION

This chapter is divided into two main parts. The first part contains different parametric studies on the powertrain itself without coupling to a specific thrust requirement or mission. The influence of specific design parameters of a fuel cell powertrain in the aviation context are evaluated individually. The second part presents the results of the specific mission analysis for different aircraft categories. For each category, the propulsion system is designed optimally considering the results of the parametric studies and mission specific design assumptions.

### 4.1 Parametric powertrain studies

The following studies focus on design parameters of the fuel cell stack itself and the heat exchanger. Assumptions for power electronics, electric motors and compressors are kept constant during all studies as presented in the appendix. Table 1 presents the investigated variations of Fuel cell type (*Type*), operating temperature (*T*), cathode stoichiometry ( $\lambda_c$ ), operating pressure (*p*), relative current density (RCD) and the heat exchanger temperature effectiveness ( $P_{\text{target}}$ ). The take-off condition (Height = 0m, Ma = 0,  $\Delta T_{ISA}=15\text{K}$ ) with a design shaft power of 1MW is selected for all designs since take-off is the most critical point for a fuel cell propulsion system.

**Table 1**  
Parameter variation in powertrain studies

	Type [-]	T [K]	$\lambda_c$ [-]	p [bar]	RCD [-]	$P_{\text{target}}$ [-]
<b>T-Study</b>	LT-/ HT-PEMFC	323.15- 353.15 / 393.15- 453.15	2	1.5	0.7	0.85
<b><math>\lambda_c</math>-Study</b>	LTPEMFC	353.15	2-6	1.5	0.7	0.85
<b>p-Study</b>	HTPEMFC	433.15	2	1.1-3	0.7	0.85
<b>RCD-Study</b>	HTPEMFC	433.15	2	1.5	0.2-0.98	0.85
<b><math>P_{\text{target}}</math>- Study</b>	HTPEMFC	433.15	2	1.5	0.7	0.43-0.85

#### 4.1.1 Operating temperature and fuel cell type

The HTPEMFC model shows a slight increase in cell voltage for rising operating temperatures but the temperature has almost no effect on the LTPEMFC. Better reaction kinetics are counterbalanced by lower reversible cell voltage in the LTPEMFC. An increase in operating temperature strongly facilitates the cooling since the temperature difference between the cooling fluid and the ambient rises.

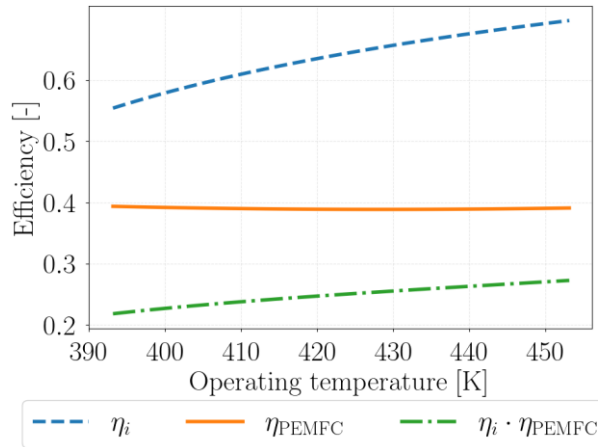


Figure 3 Operating temperature design study: Efficiency

Figure 3 shows the efficiencies of the fuel cell stack, the internal efficiency as defined in section 3.4 and the product of both using a HTPeMFC in a temperature range from 393 K to 453 K. The fuel cell efficiency is almost constant since the design point is located at  $RCD = 0.7$ . For a constant RCD the cell voltage is only slightly influenced by the temperature while the current density varies. In contrast, the internal efficiency decreases strongly from 69.7% to 55.4% with decreasing temperature. This is due to the need of higher cooling air mass flows that have to be provided by fans at take-off condition to compensate lower temperature differences. Thereby, the parasitic losses increase and finally reduce the efficiency of the system.

Moreover, this study shows that not only efficiency decreases with lower operating temperatures but also the mass of the fuel cell and cooling system increases by almost a factor of 2 when reducing operating temperature from 453 K to 393 K. This trend continues when the operating temperature is further reduced and using a LTPeMFC instead of a HTPeMFC. Below 346 K the LTPeMFC system does not converge since the required power to cool the system overcompensates the fuel cell power.

The choice of operating temperature might not be driven by slight differences in cell voltage but by the strong decrease of internal efficiency with lower temperature difference to the ambient. Therefore, high operating temperatures are preferable in the aviation context, where cooling systems have to be kept small and efficient. For the mission analysis a HTPeMFC at 453 K is used.

#### 4.1.2 Cathode stoichiometry

According to the experiments by LÖHN [27], for LTPeMFC a higher cathode stoichiometry reduces the concentration losses and enables higher current densities. Higher air mass flows at the cathode side facilitate the removal of the produced water and therefore concentration losses are less significant. For HTPeMFC, the characteristic polarization lines do not change with higher cathode stoichiometries, since the produced water is in gaseous phase and does not block the reactants flow to the electrodes as strong as liquid water does.

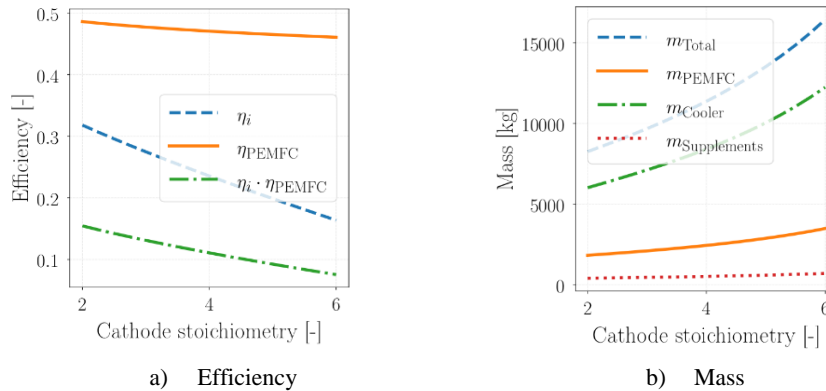


Figure 4 Cathode stoichiometry design study

A variation of cathode stoichiometry is only conducted for LTPeMFC since only a system with those fuel cells might have a benefit. Figure 4 presents the efficiencies and a mass breakdown of the powertrain in dependence on the design cathode stoichiometry. The PEMFC efficiency decreases with higher stoichiometries in Figure 4a. For a constant RCD, the current density increases from 0.57 A/cm<sup>2</sup> at  $\lambda_c = 2$  to 0.69 A/cm<sup>2</sup> at  $\lambda_c = 6$  with the stoichiometry since higher maximum current densities are achieved. At the same time the voltage drops slightly from 0.61V to 0.58V. A decrease of the RCD values would increase the cell voltage again and thereby increase the cell efficiency and is part of the study presented in chapter 4.1.4.

Figure 4b shows that the PEMFC mass rises with higher cathode stoichiometry. The rising mass can be explained by the additional parasitic losses in the compressor for the PEMFC cathode mass flow, which reduce the inner efficiency from 31.7% to 16.4%. To overcompensate this increased power losses, the system has to consist out of more

PEMFC stacks to gain 1MW net shaft power output. This leads to snowball effects that not only increase PEMFC mass, but also the mass of the cooling system and electric motors to power the compressors. In total, the mass of the power system is doubled when  $\lambda$  increases from 2 to 6.

An increase of the cathode stoichiometry above a minimum value of 2 does not improve the overall system performance. On the contrary, mass and volume of the system increase with  $\lambda$ . A reduction of  $\lambda$  may have potential to reduce parasitic losses. However, the used model is only calibrated for the investigated  $\lambda$  range and the literature review indicated that values below 2 might lead to significant concentration losses. Therefore,  $\lambda_c = 2$  is probably close to an optimum on system level and used in the mission analysis.

#### 4.1.3 Operating pressure

Similar to the cathode stoichiometry, a rising operating pressure leads to a higher cell voltage for the same current density, a higher specific power and a larger range of current densities. To reach a higher operating pressure, the air compressor for the cathode side consumes more electric power to provide the air at the required pressure level. The rising power consumption increases parasitic losses and reduces the system efficiency.

Figure 5a shows that the number of stacks has a minimum at around 2.1 bar operating pressure for a HTPEMFC with parameters described in Table 1. Below this operating pressure the number of stacks increase, since the power output per cell decreases with lower operating pressure. Above the minimum the number of stacks increase as well, since the rising parasitic compressor power loss overcomes the benefit of a better fuel cell performance. Nevertheless, the weight of the fuel cell stacks in the orange curve of Figure 5b does not show the same minimum. It increases with operating pressure instead. This is due to the assumption for the fuel cell mass. A correlation is used that calculates the fuel cell mass by the maximum possible power output of a cell ( $RCD = 1$ ). Even though the number of stacks decreases until 2.1 bar, the maximum power output increases with higher cell performance and so rises the mass. This is a little conservative assumption, but it considers that fuel cells designed for higher operating pressures might need heavier and stronger structural reinforcement.

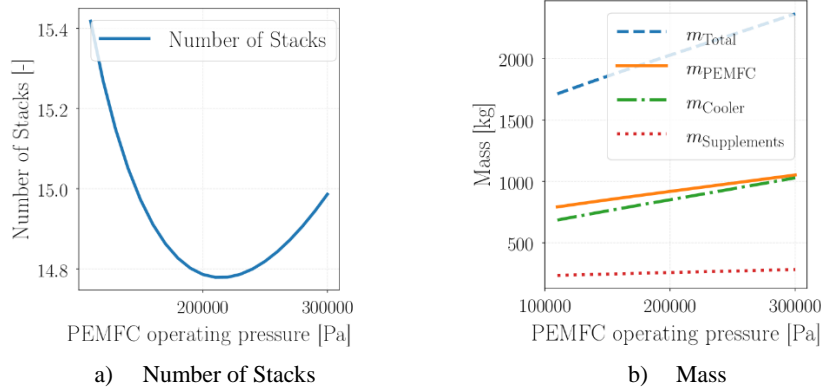


Figure 5 Operating pressure design study

The efficiencies show a similar behavior compared to the results presented for the cathode stoichiometry study in section 4.1.2. While the PEMFC efficiency only increases slightly from 38.7% at 1 bar to 39.3% at 3 bar, the internal efficiency drops strongly from 71.3% to 53.3%. The increased performance of a PEMFC with higher operating pressure does not overcome the parasitic losses of the additional compressor power requirements. This effect is even greater for higher flight altitudes, where the air has to be compressed from lower inlet pressure than at ground conditions.

The nozzle area at the cathode flow air outlet grows strongly when the pressure is reduced to 1 bar. At operating pressures below 2 bar, the nozzle reaches a point, where the flow starts to be subcritical. This forces the nozzle area to increase strongly. Since a variable

nozzle is assumed during off-design calculations, the ratio between off-design area at cruise conditions and the designed area becomes less than 10% below 1.2 bar. Such a large variance would lead to a very complex nozzle geometry. A total design operating pressure of 1.2 bar, instead of 1 bar, is chosen for the mission analysis.

This study shows that the higher cell voltage achieved by an increased operating pressure overcompensates the parasitic losses until a certain point regarding the number of PEMFC stacks. It is reasonable to keep the operating pressure low, considering the structural reinforcements and the internal efficiency drop with higher operating pressure. However, there might be other reasons, e.g. constraints imposed by the nozzle design, that favor the selection of a higher operating pressure. During cruise conditions the pressure ratio in the compressor increases compared to take-off and the effect of parasitic losses becomes stronger. Section 4.1.6 introduces some problems related to the compressor design considering cruise conditions.

#### 4.1.4 Design point location on polarization curve of the fuel cell

According to chapter 3.1 the design point location on the characteristic polarization curve of the PEMFC is set by the relative current density RCD. Figure 6a shows the effect of increasing RCD on the efficiency. Not only the stack efficiency decreases but also the inner efficiency and the total efficiency of the power system decrease from 40.6% at RCD = 0.2 to 17.7% at RCD = 1. This can be explained by the increased demand of cathode air mass flow (+129% from RCD = 0.2 to RCD = 1) and cooling air mass flow (+256% from RCD = 0.2 to RCD = 1) which increase parasitic losses in the corresponding compressors. Due to the lower efficiency of the fuel cell stack, the mass flows increase with RCD which leads to a higher consumption of oxygen (air) and hydrogen while the heat output increases as well.

At the same time increasing RCD decreases the oversizing of the fuel cell stacks. This can be seen in Figure 6b, where the blue line represents the maximal achievable electric power output of the sized fuel cell stacks (at RCD = 1) and the orange dashed line represents the actual electric power output of the fuel cell stacks. This means that at RCD = 0.2 the number of stacks is oversized by a factor of 2.9 and at RCD = 1 it is by definition not oversized at all. Since the design target is a system with 1MW net power output at take-off condition, the stack power output has to increase continuously with increasing RCD and decreasing system efficiency. As a consequence, the maximal achievable power output initially decreases with rising RCD due to less oversizing but at RCD = 0.81 a minimum is reached. For further increasing RCD the effect of lower efficiency and higher power demand outperforms the decreasing oversizing.

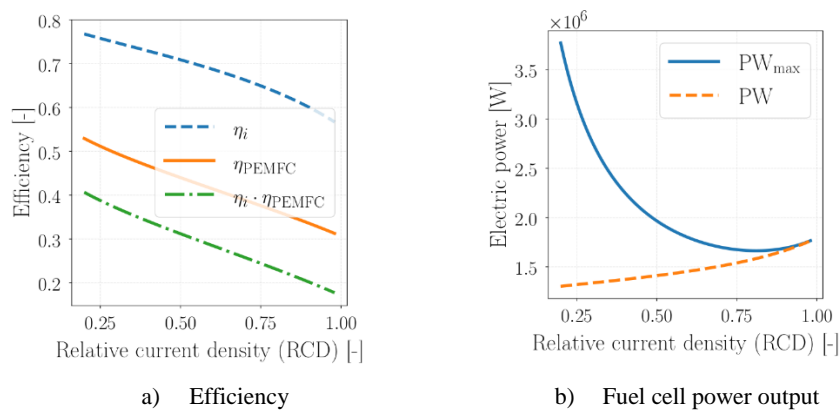


Figure 6 Variation of the relative current density at the design point

Since the mass of the PEMFC is correlated with the maximal achievable power output, the solid orange curve in Figure 7 shows the same trend as the solid blue curve in Figure 6b with a minimum at RCD = 0.81. The mass of the cooler increases strongly by more than a factor of 3.5 due to an increase of produced heat from 0.943 MW at RCD = 0.2 to 3.387 MW at RCD = 1. The total mass of the overall system (blue dashed line in Figure

7) as the sum of PEMFC stacks, cooler and assumed mass for the electric supplements has a minimum at  $RCD = 0.54$  with 1780 kg.

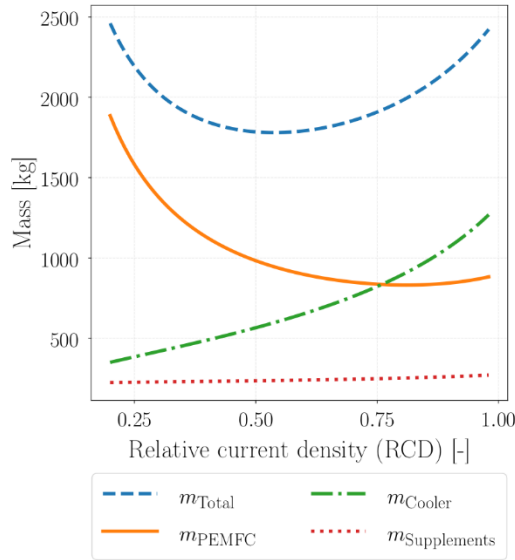


Figure 7 Component masses for a variation of the relative current density at the design point

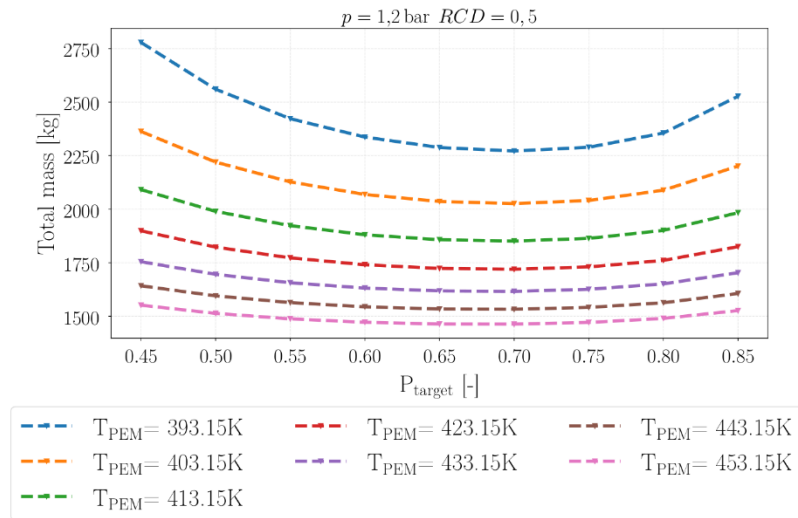
The results show that there is an RCD value for the minimal total mass of the system which should not be exceeded. Higher RCD values lead to rising mass with lower efficiency. The selection of a lower relative current density leads to an increasing efficiency. This reduces not only the consumption of hydrogen but also the weight of the hydrogen tank for a defined mission. The value of RCD with minimal total mass including the tank will shift to lower values of RCD. For this reason, the RCD that leads to a minimal system mass is evaluated during the mission analysis in chapter 4.2. Please note, the RCD value for minimal mass is only valid for the used polarization line in this model and depends on the assumptions for the mass estimation of all components. However, the qualitative results presented in this study are independent from the assumptions made.

#### 4.1.5 Design point of heat exchanger

The temperature effectiveness  $P_{target}$  at the design point sizes the heat exchanger similar to the RCD-value of the PEMFC. Figure 8 presents the total system mass for different fuel cell operating temperatures as a function of the temperature effectiveness of the heat exchanger. The minimal total mass decreases with higher operating temperature and the curve has less significant slopes. The heat exchanger effectiveness becomes less relevant with higher temperature differences to the ambient. While high values of the temperature effectiveness lead to less cooling air mass flow and parasitic losses, they are only achievable by large surfaces and thus higher mass and dimensions of the heat exchanger. Less parasitic losses lead to a decrease of the PEMFC mass due to lower power requirements. At some point, the increased heat exchanger mass outranges this effect, leading to a total mass increase. The internal efficiency of the system is reduced from 68% at  $P_{target} = 0.98$  to 4% at  $P_{target} = 0.2$ .

Larger sized PEMFC with low values for  $P_{target}$  enable lower partial loads during off-design under cruise conditions with higher temperature difference to the ambient. This leads to higher internal efficiencies in off-design compared to a design with higher values of  $P_{target}$ . Therefore, in each mission analysis in section 4.2 the effect of different temperature effectiveness during the design process on the overall flight performance is considered.

The exact position of the mass minimum and the behavior of the internal efficiency strongly depends on the assumptions made in this model. Since the heat exchanger model is a low order model, some effects might not be considered, e.g. air flow velocities and scaling effects. But the general qualitative behavior of the power system can be explained and is suitable for the potential analysis presented in this paper.

Figure 8  $P_{\text{target}}$  design study: Mass

#### 4.1.6 Off-design compressor performance

The compressor for the cathode air stream has to provide equal pressure in all flight phases since the operating pressure of the fuel cells is constant. Other than in conventional turbofan engines, the absolute pressure at the compressor outlet, not the pressure ratio, is relevant for the efficiency of the propulsion system. Therefore, an analysis of the compressor operating points in different flight phases is presented in this chapter. The used model is the same as in the design studies and the dimensioning design point is maximum take-off (MTO) with a net power output of 1 MW. An assumed end of field (EOF) operating point with 800 kW and a cruise operating point with 300 kW are compared in this study.

The MTO condition requires only a small pressure ratio in the compressor. Assuming an operating pressure of 1.2 bar and an ambient pressure of 1 bar, the pressure ratio is 1.2. At the same time, the corrected mass flow is 1.46 kg/s. The EOF operating has a higher velocity at ground level and slightly reduced net power consumption. The velocity of  $Ma = 0.2$  increases the dynamic pressure and thus the pressure ratio decreases slightly. The reduced pressure ratio diminishes parasitic power losses and therefore less corrected mass flow is needed for the same net power output. Since the power consumption is less than for MTO all effects combined reduce the corrected mass flow to 1.0 kg/s. Under cruise conditions the pressure ratio of 2.2 is significantly larger than under EOF and MTO conditions. This is due to the relatively low ambient pressure in 8000 m altitude. This increases parasitic power losses and the needed mass flow per net power output. Since it is assumed that the cruise condition only needs 30% of the take-off power output, the corrected mass flow reduces to 0.6 kg/s. All curves and operating points are depicted in Figure 9.

The plot to the right in Figure 9 is structured according to the axes of a compressor map. A critical problem regarding the operating behavior of a cathode compressor is identified. The gray area qualitatively indicates the area beyond the surge line of a compressor. The cruise operating point is clearly inside this area since this operating point lies up-left compared to the dimensioning MTO point. To reduce this problem the operating pressure during cruise conditions must be decreased or the mass flow increased significantly. Both possibilities would reduce the efficiency of the system and are therefore not suitable.

To solve this problem a more complex compression system avoiding the operating points behind the surge line is needed. The development of such a system is beyond the scope of this paper. Instead, a constant polytropic efficiency is assumed for the model and further research is needed to provide a stable compression system.



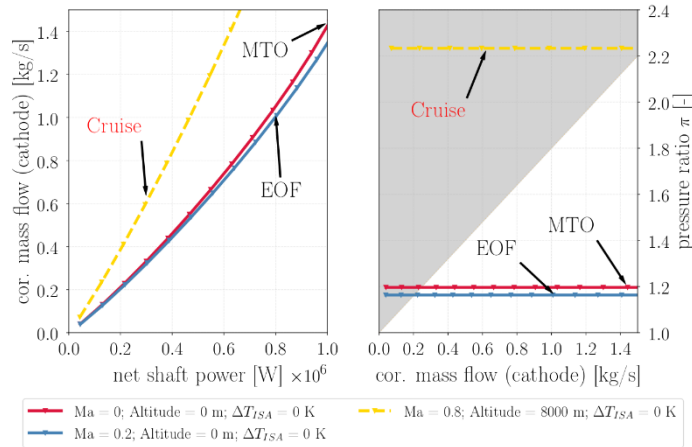


Figure 9 Cathode compressor operating points

## 4.2 Mission analysis

The PEMFC powered electric propulsion system is evaluated in a basic mission analysis for four different aircraft categories. Table 2 presents an overview of all scenarios.

**Table 2**  
Scenarios of the mission analysis

	General aviation	Commuter aircraft	Regional aircraft	Short- to Mid-range
<b>Exemplary aircraft</b>	Tecnam P2006T	Dornier 228	ATR 72	A320
<b>Mission range</b>	500 km	1280 km	1320 km	4000 km
<b>Maximal range</b>	1240 km	2361 km	3130 km	6390 km
<b>PAX</b>	3	14	68	180
<b>TOW</b>	1180 kg	6400 kg	22800	79000
<b>Propulsor</b>	2x Prop	2x Prop	2x Prop	2x Fan

The results of the regional aircraft class (e.g. ATR72) and the short- to mid-range aircraft class (e.g. A320) are presented in more detail. The general aviation class (e.g. Tecnam P2006T) and the commuter aircraft class (e.g. Dornier 228) are not presented in detail but some figures are shown in the comparison in section 4.2.3.

The propulsion system is sized for each scenario individually to reach the lowest system mass including fuel for the specified mission. Therefore, the outcome of the design studies is used for operating temperature, pressure and stoichiometry and an individual study for the system mass depending on the RCD and  $P_{\text{target}}$  in the design point is conducted. Other design targets, like a minimal fuel consumption, minimal total volume or a minimal tank weight will result in different specifications. But this is not analyzed in this paper, because the system mass might be one of the most critical parameters.

### 4.2.1 Regional aircraft scenario

The minimal system weight for the regional aircraft mission is reached by sizing the system at  $P_{\text{target}} = 0.4$  and  $\text{RCD} = 0.65$  (see Figure 10). The figure underlines the results in Sections 4.1.4 and 4.1.5, describing the trade-off in the variation of  $P_{\text{target}}$  and RCD on the system mass. Smaller values of  $P_{\text{target}}$  than shown in the plot are not valid, since not all operating points defined by the mission can be achieved in this case.



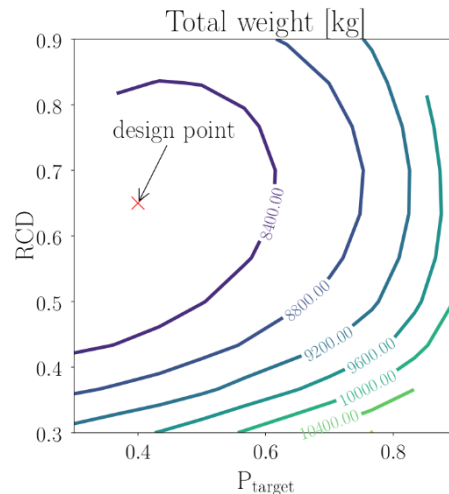


Figure 10 Regional aircraft design parameter study (Current technology level)

Using the minimal mass design, the total engine efficiency during cruise is 42%, while the fuel cells operate at 54% efficiency. 97% of the cruise thrust requirements are provided by the two electrically driven propellers. The remaining 3% are provided by the cooling and cathode air flows. For the full mission profile, 833 kg of hydrogen are needed as fuel. For this aircraft category, liquid hydrogen storage with a polyurethane insulation is the lightest tank design. The model predicts the storage structural and insulation mass with 436 kg. The columns in Figure 11 show the mass breakdown of the engine, the tank system and the total weight comparing a conventional reference system and the PEMFC engine. The assumptions and limitations of the comparison can be found in chapter 3.5. The fuel cell driven powertrain is more than six times heavier than the reference engine. Otherwise, the hydrogen storage system including buffer batteries is more than 40% lighter than the kerosene. This is basically due to the high gravimetric density of hydrogen. The volume of the hydrogen storage is more than four times larger than the volume of kerosene. The overall comparison shows that the hydrogen fuel cell driven engine is about 2 times heavier than the reference system.

Taking into consideration assumptions for a technology level with entry into service in 2040 (*EIS*), the design variable RCD moves from 0.65 to 0.6 to reach the minimal system weight. The assumption of higher fuel cell power densities enables a more oversized design without a large weight penalty but with large efficiency improvements. Total weight is reduced compared to today's technology level by about 30% to 5751 kg. Furthermore, the higher system efficiency (48,3% in cruise) reduces fuel consumption and better insulation techniques reduce tank size and weight. In addition, the size of the fuel cell stacks, cooler and other electric components is reduced. Figure 12 presents a volumetric comparison of the components with a typical regional aircraft. The comparison shows that only the hydrogen tank has to be integrated into the fuselage. Independent of the engine type, the low volumetric density might not allow any other integration when using hydrogen as fuel. The propulsion system itself might be included into the wings and a nacelle, similar to that of the reference aircraft.

However, the integration in Figure 12 is only a volumetric comparison and is not an aircraft pre-design. A detailed analysis would need to consider the full aircraft design including weight and balance, structural calculations, new thrust requirements, etc., to find a valid and good aircraft design. Conceptually new aircraft designs might be necessary to integrate a hydrogen tank into the fuselage while keeping enough space for payload.

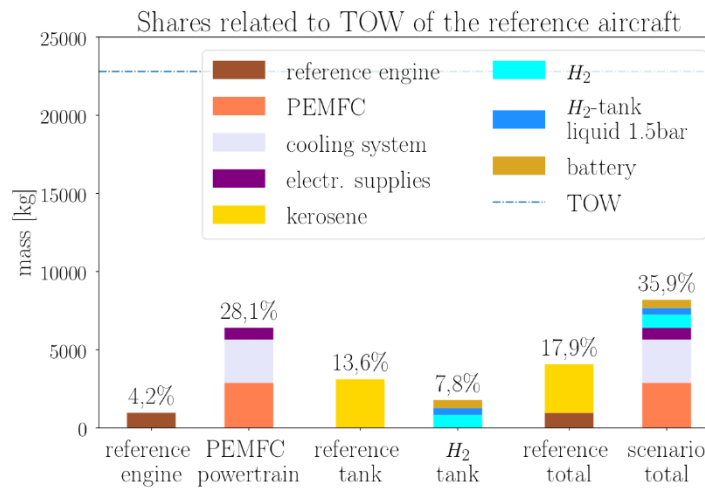


Figure 11 Regional aircraft mass breakdown (Current technology level)

Nevertheless, the presented mission analysis shows that the regional aircraft class has a high potential to integrate a fuel cell driven propulsion system. The parts of the powertrain are small enough to be integrated into the nacelle and the wing, and the fuselage size of a regional aircraft allows the integration of a tank for liquid hydrogen. Compared to the reference aircraft, the fuel cell driven aircraft would have an increase in take-off mass of 18% for today's technology level and 7.4% for EIS 2040. Since the aircraft design is not considered in this study, some snowball effects are neglected. But the deviation in mass is small enough to assume that a suitable aircraft design can be found with further detailed analysis.

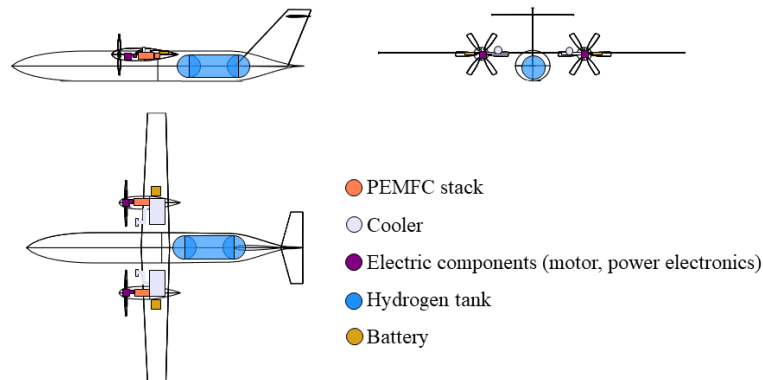


Figure 12 Regional aircraft volumetric comparison (EIS 2040)

#### 4.2.2 Short- to Mid-range scenario

The short- to mid-range scenario covers the largest aircraft class that was analyzed during the calculations for this paper. The high TOW of this class requires large powertrains with thrust above 140 kN per engine during take-off. Assuming a technology level for EIS 2040, the lightest design is found at  $RCD = 0.4$  and  $P_{target} = 0.8$ . Compared to the design values of the regional aircraft scenario ( $RCD = 0.6$ ,  $P_{target} = 0.4$ ) these values show that the larger design is driven by the heat exchanger weight and performance. A smaller RCD increases the efficiency and reduces the waste heat at the same time. In addition, a high value for  $P_{target}$  is needed to keep the cooling air mass flow in a reasonable dimension.

Figure 13 indicates that the mass of a fuel cell driven power train with assumptions for EIS 2040 is more than 8 times heavier than its reference. With 50,484 kg it has a share of

68.6% of the TOW of the reference aircraft. During cruise the total engine efficiency is 46.9% with fuel cells operating at 62.1% efficiency (on cell level). 4,293 kg of hydrogen are needed on the mission of a range of 4,000 km. Considering a liquid hydrogen tank and buffer batteries, the mass of the energy storage is 39% lower than in the reference case with kerosene as energy carrier. However, the total weight (engine + storage) increases by more than a factor of 3 when the fuel cell-based propulsion system is introduced.

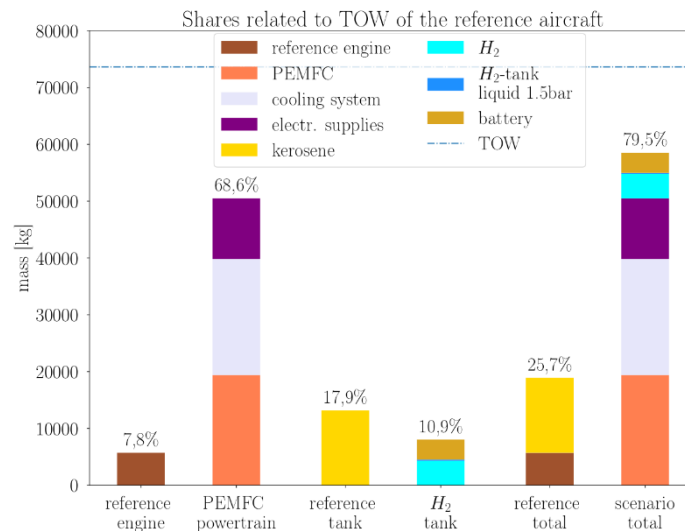


Figure 13 Short- to mid-range aircraft mass breakdown (EIS 2040)

The volumetric comparison of the components in Figure 14 shows that it is not possible to integrate the PEMFC stacks and the batteries inside the nacelle of the reference aircraft. Therefore, they are located in the fuselage in front of the hydrogen tank. This further reduces the available space for payload and increases the system complexity regarding cooling and the design of the electric circuit due to longer distances between the powertrain components. As described in section 4.2.1, this volumetric comparison is not meant to represent a realistic aircraft design, but it indicates the problems regarding the integration of the system.

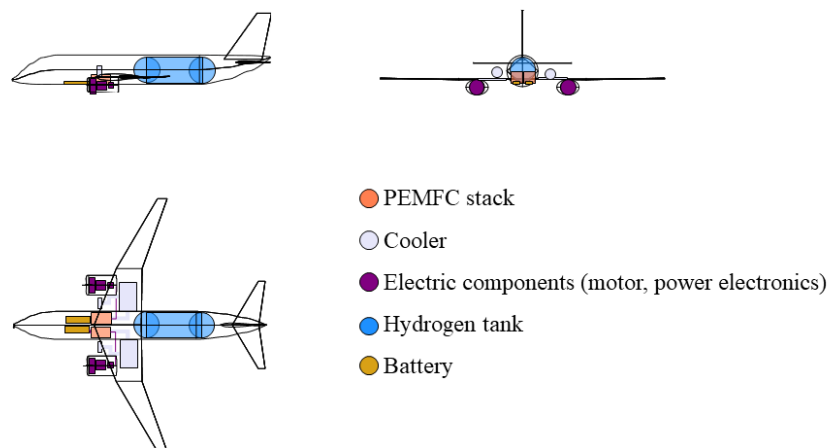


Figure 14 Short- to mid-range aircraft volumetric comparison (EIS2040)

Compared to a future technology level (total mass = 50,484 kg), the lightest possible propulsion system design with assumptions for a current technology level weighs 82,783 kg. This is more than the reference aircraft's TOW. These values show that the hydrogen

fuel cell driven propulsion system has low potential for short- to mid-range aircraft. The gravimetric and volumetric power densities of electric components, fuel cell stacks and the cooling system are too low, even with assumptions for EIS 2040. The mass and volume of the new components have a significant impact on the aircraft design. Therefore, at the moment it is unlikely to find an aircraft design in this category that enables the integration of a hydrogen fuel cell-driven engine and is capable of carrying a reasonable amount of payload at the same time over a distance of 4,000 km.

#### 4.2.3 Comparison of all scenarios

In addition to the two scenarios presented, a general aviation aircraft mission and a typical commuter aircraft mission were analyzed. They are not presented in detail in this paper, since the results show no significant new aspects compared to the already presented scenarios. However, this section compares the main outcome of all four scenarios.

Table 3 compares the results for all four scenarios with assumptions for today's technology level and improved technology for EIS 2040. In all four cases the design RCD value is reduced slightly with future technology level. This is due to the assumption of higher fuel cell power densities which enables a higher oversizing of the system to increase the cell efficiency and thus, the total efficiency of the system ( $\eta_{tot,cruise}$ ) during cruise. The  $P_{target}$  value for the cooler is chosen as the smallest value that enables operation in all flight phases according to the standard mission's flight envelope for every scenario. According to the results of section 4.1.5, high values of  $P_{target}$  are avoided to reduce the heat exchanger mass. The presented designs show that the highest overall engine efficiency is reached with the fuel cell powered propeller engine in the regional aircraft scenario.

**Table 3**  
**Results of the mission analysis for propulsion system designs with minimal mass (Current technology level / EIS 2040)**

	<b>General aviation</b>	<b>Commuter aircraft</b>	<b>Regional aircraft</b>	<b>Short- to Mid-range</b>
<b>RCD [-]</b>	0.3 / 0.25	0.5 / 0.45	0.65 / 0.6	0.5 / 0.4
<b><math>P_{target}</math> [-]</b>	0.95 / 0.95	0.8 / 0.75	0.4 / 0.4	0.85 / 0.8
<b><math>\eta_{tot,cruise}</math> [-]</b>	37.1% / 43.9%	40.1% / 46.6%	42.0% / 48.3%	41.1% / 46.9%
<b>Power density [kW / kg]</b>	0.378 / 0.596	0.537 / 0.839	0.444 / 0.715	0.405 / 0.594
<b><math>\Delta mass</math> [kg]</b>	+228 / +144	+1618 / +526	+4109 / +1677	+63887 / +39615
<b><math>\frac{\Delta mass}{TOW}</math> [-]</b>	+19.3% / +12.2%	+25.2% / +8.2%	+18.0% / +7.4%	+86.8% / +53.8%
<b>Potential</b>	moderate	moderate/high	high	low

The power densities are calculated for the take-off condition and the highest values are reached for the commuter aircraft class. The smaller aircraft (general aviation, commuter aircraft) have problems with the integration of the hydrogen tank since the fuselages are narrow and the gravimetric and volumetric efficiency of liquid hydrogen tanks is reduced. In the case of the general aviation aircraft, a compressed hydrogen tank shows better results than the liquid hydrogen tank. This is why the difference of fuel cell powertrain mass to the reference powertrain ( $\Delta mass$ ) related to take-off weight ( $\Delta mass/TOW$ ) is higher for the two small aircraft categories compared to the regional aircraft. However, they are still in a region, where new aircraft designs and further development of all components might enable a reasonable integration of a fuel cell powered engine. The potential for the integration of a hydrogen fuel cell-driven propulsion system is classified in the categories "low", "moderate" and "high". The three categories represent the

probability to find a suitable integration of the presented fuel cell system into the aircraft class, combining all results of the presented studies. In total, the potential of the general aviation and commuter aircraft class is evaluated as moderate to high. The regional aircraft scenario has the highest potential (see chapter 4.2.1) and the short- to mid-range aircraft has a low potential (see chapter 4.2.2) for the integration of the powertrain.

All values presented in the scenario analysis do not consider a variation in the aircraft design due to the integration of the fuel cell system. The effects of higher TOW and new weight distribution in the aircraft on structural and aerodynamic aspects are neglected. In addition, the use of hydrogen instead of kerosene has some general drawbacks that have to be considered. For example, the landing mass is significantly higher since the energy density of hydrogen is higher. This will probably lead to heavier landing gears. But at the same time, a fuel cell driven powertrain enables some new design options, e.g. distributed propulsion, to increase aerodynamic efficiency and reduce redundancy issues. Currently there is a lot of research that focusses on advancements of LTPEMFCs. The polarization curves used in this study may not consider the latest developments and probably underestimate the current level of technology. Since it is very difficult to foresee the development for an EIS 2040 aircraft regarding the PEMFC technology and all other related components, the assumptions made in this paper might not represent the real potential in all cases.

Nevertheless, the presented results and figures clearly indicate trends for the potential of a PEMFC powertrain for different aircraft categories. The absolute values should be evaluated relatively between the scenarios instead of being absolutely compared to real engines and aircrafts. Further studies should consider the aircraft design and the latest commercially available fuel cell technologies to develop a valid predesign model including a fuel cell driven powertrain.

## 5.0 CONCLUSION

This paper presents models for the thermodynamics of low and high temperature PEMFC stacks and a cooling system to dissipate heat to the environment. The PEMFC model is calibrated using experimental data for various operating conditions taken from the literature. The impact of different sizing parameters on the performance of the FC-based propulsion system is investigated. A set of assumptions for main system components is developed for the recent technology level and an assumed EIS in 2040. Furthermore, a model to size hydrogen tanks is included. Key targets during the design process are identified as the ability of heat removal from the PEMFC stack and the efficiency of the fuel cell stack. HTPEMFCs are found to have a higher potential since they have higher operating temperatures resulting in a high temperature difference to the ambient. Additionally, the behavior of the cathode air compressor in different aviation operating points is discussed. Cruise is a critical compressor operating point due to the operating points tendency to lie behind the surge line. Furthermore, a low operating pressure is preferable, to keep the compressor parasitic power loss small.

Furthermore, the model is used to conduct four mission analysis for different aircraft categories to identify the potential of the propulsion system for each of them. Regional aircraft show the highest potential, because the fuselage diameter enables easy integration of a cryogenic fuel cell tank. Moreover, mass and volume of the fuel cell powertrain are reasonable compared to the TOW. The assumptions for future technology level lead to an even higher potential for the regional aircraft category. In contrast, the short- to mid-range scenario offers the lowest potential. The volumetric and gravimetric power densities of the PEMFC stacks and the heat exchanger are too low compared to a gas turbine to achieve the high thrust requirements of larger aircraft even with assumptions for a future technology level.

The results presented in this paper are limited to a pure potential analysis of the system since no iterative aircraft design was made in this paper. The thrust requirements and aerodynamics are not adjusted in order to allow a feasible integration of the designed PEMFC powertrain. Nevertheless, in comparison the results show the trends of the different designs and the potential can be estimated.

Future work should include the aircraft design to consider snowball effects and benefits from fuel cell specific design options, e.g. distributed propulsion. Additionally, the fuel cell model should be updated and calibrated with the most recent state of the art fuel cell data. Significant advancements during the last years have been made especially for LTPEMFCs which might enable their application, even if the ambient temperature difference at ground is low.

## REFERENCES

- [1] JONATHAN WATTS, "Climate scientists shocked by scale of floods in Germany," *The Guardian* (16 July 2021).
- [2] IEA, "Tracking aviation 2020," International Energy Agency, <https://www.iea.org/reports/tracking-aviation-2020>.
- [3] IEA, "The Covid-19 Crisis and Clean Energy Progress: Report Extract Transportation," International Energy Agency, <https://www.iea.org/reports/the-covid-19-crisis-and-clean-energy-progress/transport#aviation>.
- [4] European Commission, *Flightpath 2050: Europe's vision for aviation*, Publ. Off. of the Europ. Union, Luxembourg, 2011.
- [5] T H BRADLEY et al., "Development and experimental characterization of a fuel cell powered aircraft," *Journal of Power Sources*, vol. 171, no. 2, pp. 793–801, 2007.
- [6] S SAHOO et al., "A Review of Concepts, Benefits, and Challenges for Future Electrical Propulsion-Based Aircraft," *Aerospace*, vol. 7, no. 4, p. 44, 2020.
- [7] H LEI and B KHANDELWAL, "Investigation of Novel Configuration of Hydrogen Micromix Combustor for Low NO<sub>x</sub> Emission," *AIAA Scitech 2020 Forum*, Orlando, FL, American Institute of Aeronautics and Astronautics, Reston, Virginia, 2020.
- [8] R MERKLER et al., "Integration aspects for large generators into turbofan engines for a turbo-electric propulsive fuselage concept," *ISABE 2019*, 2019.
- [9] M SCHRÖDER et al., "Optimal operating conditions of PEM fuel cells in commercial aircraft," *International Journal of Hydrogen Energy*, vol. 46, no. 66, pp. 33218–33240, 2021.
- [10] J KALLO, "DLR leads HY4 project for four-seater fuel cell aircraft," *Fuel Cells Bulletin*, vol. 2015, no. 11, p. 13, 2015.
- [11] HES ENERGY SYSTEMS, "HES unveils Element One hydrogen-electric passenger aircraft," *Fuel Cells Bulletin*, vol. 2018, no. 11, pp. 4–5, 2018.
- [12] A PAPAGIANNI et al., "Conceptual Design of a Hybrid Gas Turbine - Solid Oxide Fuel Cell System for Civil Aviation," *ISABE Proceedings 2019*, Canberra, Australia, 2019.
- [13] AIRBUS DEUTSCHLAND GMBH, "Liquid Hydrogen Fuelled Aircraft – System Analysis: CRYOPLANE," Sep. 2003.
- [14] A GOMEZ and H SMITH, "Liquid hydrogen fuel tanks for commercial aviation: Structural sizing and stress analysis," *Aerospace Science and Technology*, vol. 95, 2019.
- [15] D F WATERS and C P CADOU, "Engine-integrated solid oxide fuel cells for efficient electrical power generation on aircraft," *Journal of Power Sources*, vol. 284, pp. 588–605, 2015.
- [16] A CHANDAN et al., "High temperature (HT) polymer electrolyte membrane fuel cells (PEMFC) – A review," *Journal of Power Sources*, vol. 231, pp. 264–278, 2013.
- [17] M H BARGAL et al., "Liquid cooling techniques in proton exchange membrane fuel cell stacks: A detailed survey," *Alexandria Engineering Journal*, vol. 59, no. 2, pp. 635–655, 2020.
- [18] G ZHANG and S G KANDLIKAR, "A critical review of cooling techniques in proton exchange membrane fuel cell stacks," *International Journal of Hydrogen Energy*, vol. 37, no. 3, pp. 2412–2429, 2012.
- [19] T HUA et al., "Technical Assessment of Compressed Hydrogen Storage Tank Systems for Automotive Applications," Chicago, USA, Argonne National Laboratory 2010.
- [20] R P O'HAYRE et al., *Fuel cell fundamentals*, Third edition, Wiley, Hoboken New Jersey, 2016.
- [21] A J COLOZZA, "Hydrogen Storage for aircraft applications overview," Ohio, NASA 2002.
- [22] J J MINNEHAN and J W PRATT, "Practical Application Limits of Fuel Cells and Batteries for Zero Emission Vessels," Sandia National Laboratories Nov. 2017.
- [23] B HÖHLEIN, "Wasserstofflogistik - verteilen, speichern und betanken," *FVS Themen*, pp. 152–161, 2004.
- [24] D VERSTRAETE, "Long range transport aircraft using hydrogen fuel," *International Journal of Hydrogen Energy*, vol. 38, no. 34, pp. 14824–14831, 2013.

- 
- [25] S REITENBACH et al., “Design and Application of a Multidisciplinary Predesign Process for Novel Engine Concepts,” *Journal of Engineering for Gas Turbines and Power*, vol. 141, no. 1, 2019.
- [26] A DICKS and D A J RAND, *Fuel cell systems explained*, Third edition, John Wiley & Sons Inc, Hoboken, New Jersey, 2018.
- [27] H LÖHN, “Leistungsvergleich von Nieder- und Hochtemperatur-Polymerelektrolytmembran-Brennstoffzellen – Experimentelle Untersuchungen, Modellierung und numerische Simulation,” PhD thesis, TU Darmstadt, Darmstadt, Germany 2010.
- [28] Verein Deutscher Ingenieure, *VDI Heat Atlas*, Springer Berlin Heidelberg, Berlin, Heidelberg, 2010.
- [29] W M KAYS and A L LONDON, *Compact heat exchangers*, 3. ed., Krieger, Malabar, Fla., 1998.
- [30] R K SHAH and D P SEKULIC, *Fundamentals of Heat Exchanger Design*, JOHN WILEY & SONS, INC., Hoboken, 2003.



## APPENDIX

**Table 4**  
**Model assumptions (Today / EIS 2040)**

Component	Parameter	Today	EIS 2040
<b>Inlet</b>	Pres. Loss Coefficient [-]	0.99	0.99
<b>Compressor</b>	$\eta_{pol.}$ [-]	0.9	0.93
<b>PEMFC</b>	Cell surface [cm <sup>2</sup> ]	650	650
	Cells/Stack [-]	370	370
	Pres. Loss Coefficient [-]	0.95	0.95
	Cell voltage [V]	Polarization line model	+10%
	$\lambda_{Anode}$ [-]	1.2	1.2
	T <sub>H2, Tank</sub> [K]	21.15	21.15
	Vol. power density [kW/l]	3.1	4
	Grav. power density [kW/kg]	2	3
<b>Cooler</b>	Pres. Loss Coefficient [-]	0.9	0.9
	U [W/m <sup>2</sup> /K]	70	100
	$\eta_{Pump}$ [-]	0.85	0.9
	Vol. surface density [m <sup>2</sup> /m <sup>3</sup> ]	700	800
	Grav. surface density [kg/m <sup>2</sup> ]	1.08	1.0
<b>Nozzle</b>	P/P <sub>s</sub> [-]	1.03	1.03
<b>Electric motor</b>	$\eta$ [-]	0.95	0.97
	Vol. power density [kW/m <sup>3</sup> ]	5000	6500
	Grav. power density [kW/kg]	9.5	12
<b>DC/DC converter</b>	$\eta$ [-]	0.989	0.989
	Vol. power density [kW/m <sup>3</sup> ]	143000	185000
	Grav. power density [kW/kg]	62	80
<b>Power electronics</b>	$\eta$ [-]	0.975	0.975
	Vol. power density [kW/m <sup>3</sup> ]	32982	46000
	Grav. power density [kW/kg]	14.3	20
<b>Battery</b>	Vol. energy density [Wh/l]	250	375
	Grav. energy density [Wh/kg]	200	300
<b>Propeller/Fan</b>	$\eta$ [-]	Const. map	Const. map
<b>Hydrogen storage</b>	Safety factor [-]	2	2
	$\Gamma_{boiloff}$ [%/h]	0.1	0.1
	Struct. Material [-]	Al	CFK
	Struct. Mat. Density [kg/m <sup>3</sup> ]	2850	1530
	Struct. yield strength [N/mm <sup>2</sup> ]	127	1500
	Insul. Mat [-]	Polyurethan	Future foam insul.
	Insul. Mat. Density [kg/m <sup>3</sup> ]	35	35
	Insul. $\lambda$ [W/m/K]	0.006	0.003

**Table 5**  
**PEMFC polarization line model (HT / NT)**

Parameter	HTEMFC	LTEMFC
$\alpha$ [-]	0.32	0.32
$j_0(T_{PEM}, p)$ [A/cm <sup>2</sup> ]	$2 * 10^{-11} * e^{0.0355 * T_{PEM}} * \frac{p^{0.6}}{100000}$	$8 * 10^{-12} * e^{0.0437 * T_{PEM}} * \frac{p^{0.55}}{100000}$
$ASR_{ohm}$ [Ωcm <sup>2</sup> ]	0.085	0.05
$c(\lambda_c)$ [V]	0.1	$0.12 + 0.012 * (\lambda_c - 2)$
$j_0(T_{PEM}, p, \lambda_c)$ [A/cm <sup>2</sup> ]	$(1.17 + 0.0094 * (T_{PEM} - 393.15)) * \frac{p^{0.35}}{100000}$	$0.9 * \frac{p^{0.3838}}{100000} * \frac{\lambda_c^{0.29}}{2}$